Title

In vivo imaging of human photoreceptor mosaic with wavefront sensorless adaptive optics optical coherence tomography

Journal

Biomedical Optics Express, 6(2)

ISSN

2156-7085

Authors

Wong, Kevin SK
Jian, Yifan
Cua, Michelle
et al.

Publication Date

2015-02-01

DOI

10.1364/boe.6.000580

Peer reviewed

In vivo imaging of human photoreceptor mosaic with wavefront sensorless adaptive optics optical coherence tomography

Kevin S. K. Wong,[1,5] Yifan Jian,[1,5] Michelle Cua,[1] Stefano Bonora,[2] Robert J. Zawadzki,[3,4] Marinko V. Sarunic[1,*]

[1]*Engineering Science, Simon Fraser University, Burnaby, BC, V5A 1S6 Canada*
[2]*CNR-Institute of Photonics and Nanotechnology, via Trasea 7, 35131, Padova, Italy*
[3]*UC Davis RISE Small Animal Ocular Imaging Facility, Department of Cell Biology and Human Anatomy, University of California Davis, Davis, CA 95616 USA*
[4]*Vision Science and Advanced Retinal Imaging laboratory (VSRI), Department of Ophthalmology & Vision Science, University of California Davis, Sacramento, CA 95817 USA*
[5]*These authors contributed equally to this work.*
[*]*msarunic@sfu.ca*

Abstract: Wavefront sensorless adaptive optics optical coherence tomography (WSAO-OCT) is a novel imaging technique for *in vivo* high-resolution depth-resolved imaging that mitigates some of the challenges encountered with the use of sensor-based adaptive optics designs. This technique replaces the Hartmann Shack wavefront sensor used to measure aberrations with a depth-resolved image-driven optimization algorithm, with the metric based on the OCT volumes acquired in real-time. The custom-built ultrahigh-speed GPU processing platform and fast modal optimization algorithm presented in this paper was essential in enabling real-time, *in vivo* imaging of human retinas with wavefront sensorless AO correction. WSAO-OCT is especially advantageous for developing a clinical high-resolution retinal imaging system as it enables the use of a compact, low-cost and robust lens-based adaptive optics design. In this report, we describe our WSAO-OCT system for imaging the human photoreceptor mosaic *in vivo*. We validated our system performance by imaging the retina at several eccentricities, and demonstrated the improvement in photoreceptor visibility with WSAO compensation.

OCIS codes: (110.4500) Optical coherence tomography; (010.1080) Active or adaptive optics; (220.1000) Aberration compensation; (170.0110) Imaging systems; (170.4470) Ophthalmology; (120.3890) Medical optics instrumentation

References and links

1. J. Liang, D. R. Williams, and D. T. Miller, "Supernormal vision and high-resolution retinal imaging through adaptive optics," J. Opt. Soc. Am. A **14**(11), 2884–2892 (1997).
2. R. J. Zawadzki, S. M. Jones, S. S. Olivier, M. Zhao, B. A. Bower, J. A. Izatt, S. Choi, S. Laut, and J. S. Werner, "Adaptive-optics optical coherence tomography for high-resolution and high-speed 3D retinal in vivo imaging," Opt. Express **13**(21), 8532–8546 (2005).
3. J. Porter, H. M. Queener, J. E. Lin, K. Thorn, and A. Awwal, eds., *Adaptive Optics for Vision Science* (John Wiley & Sons, Inc., 2006).
4. P. Godara, A. M. Dubis, A. Roorda, J. L. Duncan, and J. Carroll, "Adaptive Optics Retinal Imaging: Emerging Clinical Applications," Optom. Vis. Sci. **87**(12), 930–941 (2010).
5. D. R. Williams, "Imaging single cells in the living retina," Vision Res. **51**(13), 1379–1396 (2011).
6. Y. Geng, A. Dubra, L. Yin, W. H. Merigan, R. Sharma, R. T. Libby, and D. R. Williams, "Adaptive optics retinal imaging in the living mouse eye," Biomed. Opt. Express **3**, 715–734 (2012).
7. F. Felberer, J.-S. Kroisamer, B. Baumann, S. Zotter, U. Schmidt-Erfurth, C. K. Hitzenberger, and M. Pircher, "Adaptive optics SLO/OCT for 3D imaging of human photoreceptors in vivo," Biomed. Opt. Express **5**(2), 439–456 (2014).

8. X. Zhou, P. Bedggood, and A. Metha, "Improving high resolution retinal image quality using speckle illumination HiLo imaging," Biomed. Opt. Express **5**(8), 2563–2579 (2014).
9. G. Palczewska, Z. Dong, M. Golczak, J. J. Hunter, D. R. Williams, N. S. Alexander, and K. Palczewski, "Noninvasive two-photon microscopy imaging of mouse retina and retinal pigment epithelium through the pupil of the eye," Nat. Med. **20**(7), 785–789 (2014).
10. M. Zacharria, B. Lamory, and N. Chateau, "Biomedical imaging: New view of the eye," Nat. Photonics **5**(1), 24–26 (2011).
11. M. Pircher, B. Baumann, E. Götzinger, H. Sattmann, and C. K. Hitzenberger, "Simultaneous SLO/OCT imaging of the human retina with axial eye motion correction," Opt. Express **15**(25), 16922–16932 (2007).
12. J. Carroll, S. S. Choi, and D. R. Williams, "In vivo imaging of the photoreceptor mosaic of a rod monochromat," Vision Res. **48**(26), 2564–2568 (2008).
13. A. Roorda, "Applications of Adaptive Optics Scanning Laser Ophthalmoscopy," Optom. Vis. Sci. **87**(4), 260–268 (2010).
14. D. Scoles, Y. N. Sulai, C. S. Langlo, G. A. Fishman, C. A. Curcio, J. Carroll, and A. Dubra, "In Vivo Imaging of Human Cone Photoreceptor Inner Segments," Invest. Ophthalmol. Vis. Sci. **55**(7), 4244–4251 (2014).
15. O. P. Kocaoglu, S. Lee, R. S. Jonnal, Q. Wang, A. E. Herde, J. C. Derby, W. Gao, and D. T. Miller, "Imaging cone photoreceptors in three dimensions and in time using ultrahigh resolution optical coherence tomography with adaptive optics," Biomed. Opt. Express **2**(4), 748–763 (2011).
16. Y. Zhang, J. Rha, R. Jonnal, and D. Miller, "Adaptive optics parallel spectral domain optical coherence tomography for imaging the living retina," Opt. Express **13**(12), 4792–4811 (2005).
17. A. G. Podoleanu and R. B. Rosen, "Combinations of techniques in imaging the retina with high resolution," Prog. Retin. Eye Res. **27**(4), 464–499 (2008).
18. R. S. Jonnal, O. P. Kocaoglu, Q. Wang, S. Lee, and D. T. Miller, "Phase-sensitive imaging of the outer retina using optical coherence tomography and adaptive optics," Biomed. Opt. Express **3**(1), 104–124 (2012).
19. Y. Jian, R. J. Zawadzki, and M. V. Sarunic, "Adaptive optics optical coherence tomography for in vivo mouse retinal imaging," J. Biomed. Opt. **18**(5), 056007 (2013).
20. O. P. Kocaoglu, R. D. Ferguson, R. S. Jonnal, Z. Liu, Q. Wang, D. X. Hammer, and D. T. Miller, "Adaptive optics optical coherence tomography with dynamic retinal tracking," Biomed. Opt. Express **5**(7), 2262–2284 (2014).
21. M. Pircher, B. Baumann, E. Götzinger, and C. K. Hitzenberger, "Retinal cone mosaic imaged with transverse scanning optical coherence tomography," Opt. Lett. **31**(12), 1821–1823 (2006).
22. B. Potsaid, I. Gorczynska, V. J. Srinivasan, Y. Chen, J. Jiang, A. Cable, and J. G. Fujimoto, "Ultrahigh speed spectral / Fourier domain OCT ophthalmic imaging at 70,000 to 312,500 axial scans per second," Opt. Express **16**(19), 15149–15169 (2008).
23. T. Schmoll, C. Kolbitsch, and R. A. Leitgeb, "Ultra-high-speed volumetric tomography of human retinal blood flow," Opt. Express **17**(5), 4166–4176 (2009).
24. M. Pircher, E. Götzinger, H. Sattmann, R. A. Leitgeb, and C. K. Hitzenberger, "In vivo investigation of human cone photoreceptors with SLO/OCT in combination with 3D motion correction on a cellular level," Opt. Express **18**(13), 13935–13944 (2010).
25. J. Porter, H. Queener, J. Lin, K. Thorn, and A. A. S. Awwal, *Adaptive Optics for Vision Science: Principles, Practices, Design and Applications* (Wiley- Interscience, 2006).
26. R. J. Zawadzki, S. M. Jones, S. Pilli, S. Balderas-Mata, D. Y. Kim, S. S. Olivier, and J. S. Werner, "Integrated adaptive optics optical coherence tomography and adaptive optics scanning laser ophthalmoscope system for simultaneous cellular resolution in vivo retinal imaging," Biomed. Opt. Express **2**(6), 1674–1686 (2011).
27. A. Dubra and Y. Sulai, "Reflective afocal broadband adaptive optics scanning ophthalmoscope," Biomed. Opt. Express **2**(6), 1757–1768 (2011).
28. A. Dubra, Y. Sulai, J. L. Norris, R. F. Cooper, A. M. Dubis, D. R. Williams, and J. Carroll, "Noninvasive imaging of the human rod photoreceptor mosaic using a confocal adaptive optics scanning ophthalmoscope," Biomed. Opt. Express **2**(7), 1864–1876 (2011).
29. S.-H. Lee, J. S. Werner, and R. J. Zawadzki, "Improved visualization of outer retinal morphology with aberration cancelling reflective optical design for adaptive optics - optical coherence tomography," Biomed. Opt. Express **4**(11), 2508–2517 (2013).
30. F. Felberer, J.-S. Kroisamer, C. K. Hitzenberger, and M. Pircher, "Lens based adaptive optics scanning laser ophthalmoscope," Opt. Express **20**(16), 17297–17310 (2012).
31. M. J. Booth, "Wavefront sensorless adaptive optics for large aberrations," Opt. Lett. **32**, 2006–2008 (2007).
32. D. Débarre, E. J. Botcherby, M. J. Booth, and T. Wilson, "Adaptive optics for structured illumination microscopy," Opt. Express **16**(13), 9290–9305 (2008).
33. N. Ji, D. E. Milkie, and E. Betzig, "Adaptive optics via pupil segmentation for high-resolution imaging in biological tissues," Nat. Methods **7**(2), 141–147 (2010).
34. D. E. Milkie, E. Betzig, and N. Ji, "Pupil-segmentation-based adaptive optical microscopy with full-pupil illumination," Opt. Lett. **36**(21), 4206–4208 (2011).
35. H. Hofer, N. Sredar, H. Queener, C. Li, and J. Porter, "Wavefront sensorless adaptive optics ophthalmoscopy in the human eye," Opt. Express **19**(15), 14160–14171 (2011).

36. Y. Jian, J. Xu, M. A. Gradowski, S. Bonora, R. J. Zawadzki, and M. V. Sarunic, "Wavefront sensorless adaptive optics optical coherence tomography for in vivo retinal imaging in mice," Biomed. Opt. Express **5**(2), 547–559 (2014).
37. S. Bonora and R. J. Zawadzki, "Wavefront sensorless modal deformable mirror correction in adaptive optics: optical coherence tomography," Opt. Lett. **38**(22), 4801–4804 (2013).
38. A. Gullstrand, ""Appendix II," in Handbuch der Physiologischen Optik, 3rd ed," Opt. Soc. Am. 1924 **1**, 351–352 (1909).
39. Y. Le Grand and S. G. El Hage, "Physiological Optics," Springer Ser. Opt. Sci. (1980).
40. W. Drexler and J. G. Fujimoto, eds., *Optical Coherence Tomography: Technology and Applications* (Springer-Verlag, 2008).
41. J. Li, P. Bloch, J. Xu, M. V. Sarunic, and L. Shannon, "Performance and scalability of Fourier domain optical coherence tomography acceleration using graphics processing units," Appl. Opt. **50**(13), 1832–1838 (2011).
42. Y. Jian, K. Wong, and M. V. Sarunic, "Graphics processing unit accelerated optical coherence tomography processing at megahertz axial scan rate and high resolution video rate volumetric rendering," J. Biomed. Opt. **18**(2), 026002 (2013).
43. J. Xu, K. Wong, Y. Jian, and M. V. Sarunic, "Real-time acquisition and display of flow contrast using speckle variance optical coherence tomography in a graphics processing unit," J. Biomed. Opt. **19**(2), 026001 (2014).
44. J. Porter, A. Guirao, I. G. Cox, and D. R. Williams, "Monochromatic aberrations of the human eye in a large population," J. Opt. Soc. Am. A **18**(8), 1793–1803 (2001).
45. J. F. Castejón-Mochón, N. López-Gil, A. Benito, and P. Artal, "Ocular wave-front aberration statistics in a normal young population," Vision Res. **42**(13), 1611–1617 (2002).
46. T. O. Salmon and C. van de Pol, "Normal-eye Zernike coefficients and root-mean-square wavefront errors," J. Cataract Refract. Surg. **32**(12), 2064–2074 (2006).
47. W. Wieser, B. R. Biedermann, T. Klein, C. M. Eigenwillig, and R. Huber, "Multi-Megahertz OCT: High quality 3D imaging at 20 million A-scans and 4.5 GVoxels per second," Opt. Express **18**(14), 14685–14704 (2010).
48. T. Klein, W. Wieser, L. Reznicek, A. Neubauer, A. Kampik, and R. Huber, "Multi-MHz retinal OCT," Biomed. Opt. Express **4**(10), 1890–1908 (2013).
49. O. P. Kocaoglu, T. L. Turner, Z. Liu, and D. T. Miller, "Adaptive optics optical coherence tomography at 1 MHz," Biomed. Opt. Express **5**(12), 4186 (2014).
50. D. C. Chen, S. M. Jones, D. A. Silva, and S. S. Olivier, "High-resolution adaptive optics scanning laser ophthalmoscope with dual deformable mirrors," J. Opt. Soc. Am. A **24**(5), 1305–1312 (2007).
51. R. J. Zawadzki, S. S. Choi, S. M. Jones, S. S. Oliver, and J. S. Werner, "Adaptive optics-optical coherence tomography: optimizing visualization of microscopic retinal structures in three dimensions," J. Opt. Soc. Am. A **24**(5), 1373–1383 (2007).
52. C. Li, N. Sredar, K. M. Ivers, H. Queener, and J. Porter, "A correction algorithm to simultaneously control dual deformable mirrors in a woofer-tweeter adaptive optics system," Opt. Express **18**(16), 16671–16684 (2010).
53. W. Zou, X. Qi, and S. A. Burns, "Woofer-tweeter adaptive optics scanning laser ophthalmoscopic imaging based on Lagrange-multiplier damped least-squares algorithm," Biomed. Opt. Express **2**(7), 1986–2004 (2011).

1. Introduction

The use of adaptive optics (AO) is essential for high-resolution, *in vivo* retinal imaging with large numerical aperture (NA) (large imaging pupil) [1–9]. AO has been combined with various ocular imaging techniques in order to achieve diffraction-limited resolution by correcting optical aberrations; fundus photography [10] and Scanning Laser Ophthalmoscopy (SLO) [11–14] are two examples of biomedical applications with AO allowing reliable imaging of cone and rod photoreceptor mosaics. Optical Coherence Tomography (OCT) has also been combined with AO to achieve high-resolution volumetric imaging [7,11,15–20]. Although conventional imaging systems have been demonstrated to be capable of imaging photoreceptor cones in healthy subjects without application of adaptive optics [21–24], the cone mosaic cannot be reliably imaged at retinal eccentricities near the fovea (<2°) or in patients with ocular defects and large aberrations.

Retinal imaging with a large NA inherently amplifies the impact of ocular aberrations from the subject's eye, which compromises the best-achievable resolution. The goal of AO is to compensate for these optical aberrations with an adaptive element, such as a deformable mirror (DM), which is conventionally controlled by a wavefront sensor (WFS) connected in a feedback AO correction loop. Closed-loop AO configurations with a wavefront sensor have been proven successful in many adaptive optics systems, and are being used in most AO ophthalmoscopes to date. However, some issues associated with the wavefront sensors, such as the non-common path aberrations, wavefront spot centroiding and wavefront

reconstruction errors, could lead to poor AO correction performance if not accounted for [25]. Another limitation with using a WFS is the sensitivity to back-reflections. Most AO systems use spherical-mirror telescopes to mitigate the back-reflections [20,26–29]. However, the use of spherical mirrors in off-axis configurations results in large system aberrations, which is often reduced by using long focal length mirrors. With these modifications, non-planar folding of the spherical-mirror telescopes is a strategic approach to minimize the system aberrations, and human rod and fovea cone photoreceptors have been imaged and resolved by such an AO-SLO system [27]. A lens-based AO-SLO design using polarization techniques to reduce back reflection in the WFS was presented as an alternative to spherical mirror based systems [30]. This approach achieved similar performance as non-planar folding telescopes.

Wavefront sensorless adaptive optics (WSAO) has been demonstrated to be a robust strategy for circumventing the limitations associated with conventional sensor-based AO systems. WSAO was first demonstrated in microscopy to correct low order aberrations [31–34]. The sensorless adaptive optics technique has been adapted into a human *in vivo* SLO imaging system, and was quantitatively compared with the corresponding wavefront-sensor-based AO-SLO [35]. The authors used a stochastic optimization method to implement the sensorless AO. Although the convergence time of the sensorless approach was relatively long, the authors demonstrated that image-based wavefront sensorless control is capable of producing images of at least comparable quality to those acquired using wavefront sensor-based SLO [35].

In our previous report, we demonstrated a WSAO-OCT system for small animal imaging that was presented and evaluated on pigmented and albino mice [36]. We developed the WSAO-OCT technique using a modal control of the DM [37], which enabled a faster convergence rate in comparison to a stochastic approach. The system had an A-scan acquisition rate of 100 kHz, and the entire optimization process required about 60 seconds. While this acquisition and optimization rate was sufficient for imaging anesthetized mice, it was not fast enough for reliable *in vivo* human retinal imaging due to involuntary eye and head movements, blinks, and the subject's fatigue.

In this report, we describe our WSAO-OCT system for *in vivo* imaging of the photoreceptor layer in the human retina. We first describe the design of our WSAO-OCT optical system and real-time data acquisition and processing platform. Next, we describe our WSAO-OCT optimization process tailored for human retinal imaging. Lastly, we present *en face* images of the human photoreceptor mosaic reconstructed from the OCT volumes acquired *in vivo* near the optic nerve head and at various retinal eccentricities along the superior meridian.

2. Methods

The details of the hardware used in our WSAO FD-OCT optical system, as well as the software used for operating the OCT engine, are presented in the following subsections. All research procedures were performed in accordance with the Declaration of Helsinki and the study protocol was approved by the institutional review board of Simon Fraser University. Human imaging was performed in healthy subjects with low-degree myopia and a large pupil in a dimly lit environment. The subjects gave written informed consent before participating in the study. The subjects' pupils were not dilated for the imaging sessions performed for this research. The subjects' non-mydriatic pupil was measured to be 6-7 mm in diameter during imaging conditions.

2.1 Optical design

Figure 1 presents a schematic of our lens-based WSAO-OCT system. Our adaptive optics setup consisted of a superluminescent diode (Superlum, Carrigtwohill, Ireland), a line scan camera (Basler, Ahrensburg, Germany), and a 5-μm-stroke PT111 MEMS deformable mirror with 37 segments and 111 actuators (Iris AO, Berkeley, CA). The light source had a center

wavelength of 830 nm and a full width at half maximum (FWHM) of 80 nm (equivalent to an axial resolution of ~2.9 µm in tissue). The optical power incident at the eye pupil was ~350 µW, which is below the Maximum Permissible Exposure based on ANSI limit at this wavelength. The conjugate plane between telescopes L7/L8 and L9/L10 in Fig. 1 was used for placing trial lenses as a means of reducing defocus and astigmatism to ensure efficient use of the DM stroke for correcting higher order aberrations. A hot mirror was used to couple an external fixation target into the system. The Gullstrand-LeGrand model of the human eye [38,39] was used for approximating the average focal length to be f_{eye} = 22.2 mm. The $1/e^2$ beam diameter at the eye pupil was ~5.5 mm. Assuming a refractive index of n = 1.33 for water at 830 nm, the theoretical NA is 0.16, which results in a $1/e^2$ waist of 1.6 µm at the retina, or a FWHM spot size of 1.9 µm. The depth of focus defined using the axial FWHM, as described in [40], was ~70 µm. In order to mitigate involuntary head movement, we constructed a bite bar with a dental impression tray to secure the upper jaw, and a forehead rest for support. This design provided external support for the subject to relax their head throughout the entire imaging session.

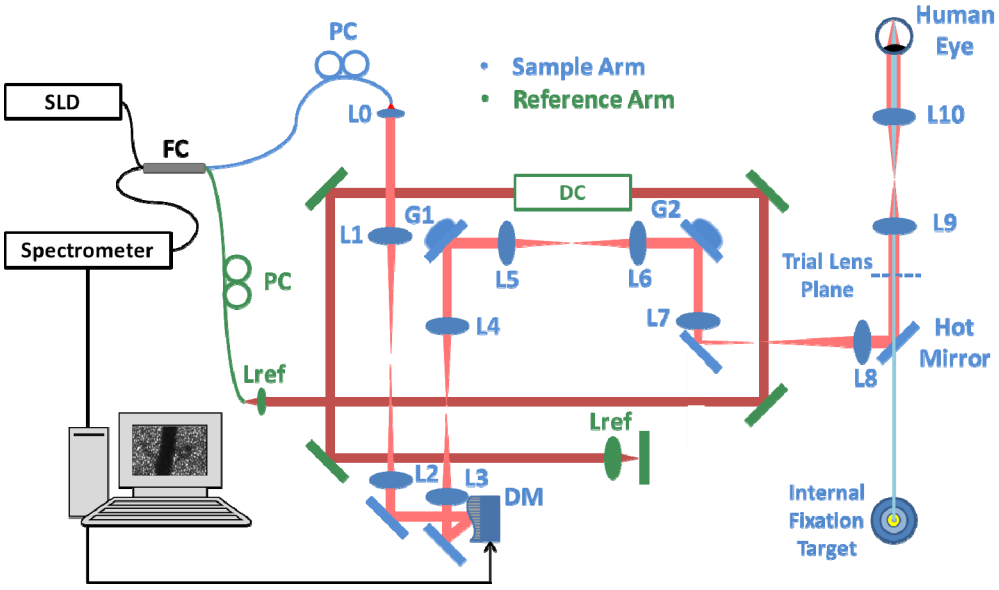

Fig. 1. Schematic of the WSAO-OCT system: DM, Deformable Mirror; SLD, Superluminescent Diode; FC, 90/10 reference/sample Fiber Coupler; G1, G2, horizontal and vertical galvanometer scanning mirrors; PC, polarization controller; DC, dispersion compensation; L0: f = 16 mm; L1, L2: f = 300 mm; L3, L4: f = 200 mm, L5, L6: f = 150 mm; L7: f = 200 mm; L8: f = 250 mm; L9: two lenses f = 200 and f = 300 mm (equivalent to f = 120 mm); L10: two lenses of f = 300 mm (equivalent to f = 150 mm). All lenses were achromatic doublets. A trial lens plane optically conjugated to the eye pupil plane is available for inserting corrective lenses for correcting defocus.

2.2 Workstation and software specifications

A modified version of the open-sourced Graphics Processing Unit (GPU)-based FD-OCT program [41,42] was used in this research. As previously presented, a dynamic depth selection option and system controls for the DM were added to the software for enabling WSAO [36]. The GPU used during imaging was the Quadro K6000 (NVIDIA, Santa Clara, California) and was capable of achieving a 1024-point-A-scan processing rate of 1.9 MHz [43]. The ultrahigh-speed FD-OCT processing rate enabled real-time generation of volumetric images and extraction of maximum intensity projection *en face* images to be used as an image-based metric for AO optimization.

2.3 Image acquisition and optimization

Our OCT engine was configured to acquire A-scans at a rate of 200 kHz. The camera was triggered to acquire at an 80% duty cycle of the cycloidal raster scan pattern to eliminate fly-back artifacts. The volume acquisition size (1024x200x80 voxels) was selected to obtain a balance between sampling density and acquisition speed with consideration to the limitations of the speed of the galvanometer-scanning mirrors. This resulted in an acquisition rate of 800 frames per second, equivalent to 10 volumes per second with processing and display in real-time. The WSAO optimization algorithm for human imaging was modified from our previous report on imaging mice [36]. For a pupil size of ~5 mm, correction of the fifth Zernike radial order has relatively low impact on the total RMS of the ocular aberrations for human imaging [44–46]. Therefore, only Zernike radial orders 2 to 4 (Zernike modes 3 to 14) were optimized to maintain a balance between optimization time and effective aberration correction. For each Zernike mode, the optimization was performed by acquiring an OCT volume for 5 different coefficient values ranging from ± 80 nm for the 2nd order radial Zernike modes and ± 48 nm for the higher modes. *En face* images at the layer of interest from these 5 volumes were extracted, and the coefficient that produced the brightest image was selected as the optimized value. If the brightest image corresponded to the coefficient at the edge of the search range, the algorithm performed a second search iteration with an additional set of 5 data points, with the coefficient range shifted in the direction of the best correction. The entire optimization process required 6~12 seconds, depending on the amount of the aberrations in the subject's eye.

3. Results

3.1 WSAO-OCT image resolution

To evaluate the quality of our optical system before aberration correction, we placed an imaging phantom, consisting of a 30 mm focal length air-spaced achromatic lens and a US Air Force (USAF) resolution target, in place of the human eye in the sample arm. We imaged groups 6 and 7 of the USAF with a flattened deformable mirror. The acquired volumes consisted of 1024x200x80 voxels to simulate imaging conditions. The spot size of our system for the phantom in air had a $1/e^2$ waist of 2.9 μm; this was sufficient for resolving group 7 element 4 (line width of 2.76 μm) shown in Fig. 2.

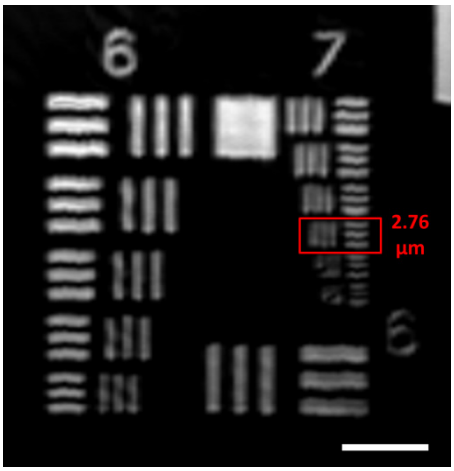

Fig. 2. Experimental quantification of the lateral resolution using a resolution target and a 30 mm focal length air-spaced achromatic lens. The achievable lateral resolution was 2.76 μm with a volume size of 1024x200x80. Scale bar: 50 μm.

3.2 Human retinal imaging with WSAO-OCT

As a demonstration of our WSAO-OCT system performance for *in vivo* human retinal imaging, we present images acquired before, during, and after the optimization process. Prior to WSAO optimization, the subject was stabilized with the head mount and fixation target. Lens L10 was manually positioned to maximize the intensity of the photoreceptor layer. Figure 3 shows the selected *en face* projection during the optimization of Zernike mode 3 (astigmatism) from an imaging session of Subject 1. To demonstrate the principle of the modal wavefront sensorless algorithm, only one Zernike mode was optimized for this data set, but with finer optimization steps (15 steps acquired, but only the even-numbered steps are included in the montage presented in Fig. 3). The sequence of images recorded for the optimization of Zernike mode 3 is provided in Media 1. The Gaussian-filtered *en face* projection shown in panel A was generated from the region between the red lines in the B-scans, as shown in panel B. The 2D Fourier transform of the *en face* images are shown in panel C. As the optimization proceeds, the intensity of the B-scan and *en face* image gradually increases to a maximum as the optimum Zernike value is found (step 6 in Fig. 3), and then decreases when moving away from it; the visibility of Yellott's ring in the Fourier transform images follows the same trend.

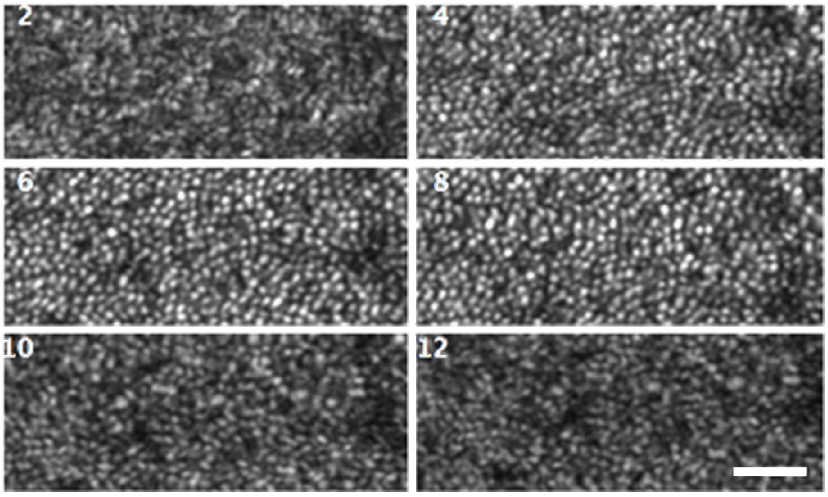

Fig. 3. Selected *en face* projection images during the optimization of Zernike mode 3 (astigmatism) in Media 1. Images of the photoreceptor mosaic were acquired at an eccentricity of ~3.0° in a non-mydriatic pupil. The field of view is 1.0°x0.4° for all images. The scale bar is 50 μm.

A comparison of the *en face* cone mosaic acquired from Subject 1 before and after optimization of all Zernike terms is presented in Fig. 4. The images were processed identically, allowing direct comparison. Following optimization, the *en face* image is brighter, and the cone mosaic is clearly visualized.

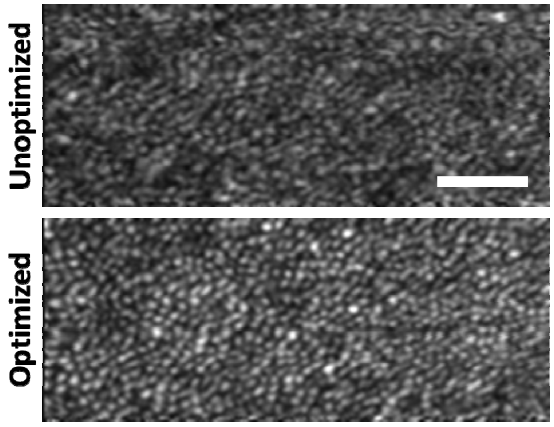

Fig. 4. Cone mosaic of Subject 1 imaged at retinal eccentricity of ~3.0°. The field of view is 1.0°x0.4°. Scale bar is 50 μm.

The complete WSAO-OCT optimization was recorded for Subject 2. Media 2 presents the real-time optimization process on the photoreceptor layer at a region near the optic nerve head. In this video, a ten-second sequence of unoptimized *en face* images at the inner and outer segment (IS/OS) and retinal pigment epithelium (RPE) layers are presented. The optimization then proceeds, where periodic fluctuations in intensity with an increasing trend can be observed. An indication of the concurrent Zernike mode being optimized as a function of time was included in the video for illustration purposes. The resolution gradually increases throughout the optimization until individual cone photoreceptors can be clearly resolved as bright circular structures. After WSAO optimization, a ten-second sequence of real-time optimized *en face* images is included for comparison. The shadows of blood vessels are landmarks for determining the motion of the subject; with modest amount of motion the optimization algorithm was still capable of performing aberration correction.

A set of B-scan and *en face* images before and after WSAO optimization from Media 2 is presented in Fig. 5. The *en face* images were generated by maximum intensity projection of the voxels within the IS/OS layer (layer 2 on the A-scan plots). The improvement in intensity after optimization is also apparent in the line profiles of A-scan (red and green boxes). The value of the optimized Zernike coefficient for each mode (representing the shape of the DM after optimization), and the corresponding increase in merit function are also presented in Fig. 5.

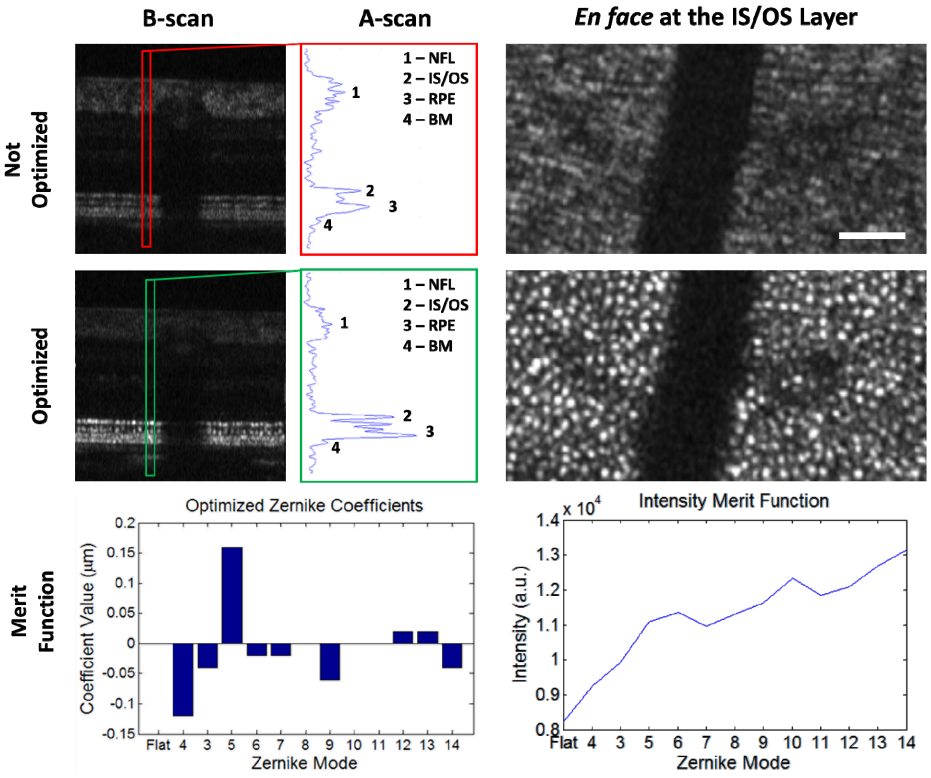

Fig. 5. Comparison of the photoreceptor visibility in the *en face* image before and after WSAO optimization. The left column is a comparison of B-scans, and the right column is a comparison of the *en face* images generated at the IS/OS layer. NFL, Nerve Fiber Layer; IS/OS, Inner and Outer Segment; RPE, Retina Pigment Epithelium; BM, Bruch's Membrane. The field of view is 1.3°x0.6° for the *en face* images. Scale bar is 50 μm. A real-time optimization video has been included in Media 2.

In order to demonstrate our system's capability of resolving the photoreceptor mosaic near the fovea, we present *en face* images acquired at four different retinal eccentricities from Subject 2. Each image was acquired after re-optimizing the ocular aberrations at the corresponding retinal location. Figure 6 provides a comparison between un-optimized and optimized *en face* images acquired at these locations. In the un-optimized images, the cones are mostly indistinguishable from speckle pattern. After optimization, the image contrast increased, and the cone mosaic can be resolved at eccentricities as close as 1.0° from the fovea. In these *en face* images, the fovea is located toward the bottom left corner.

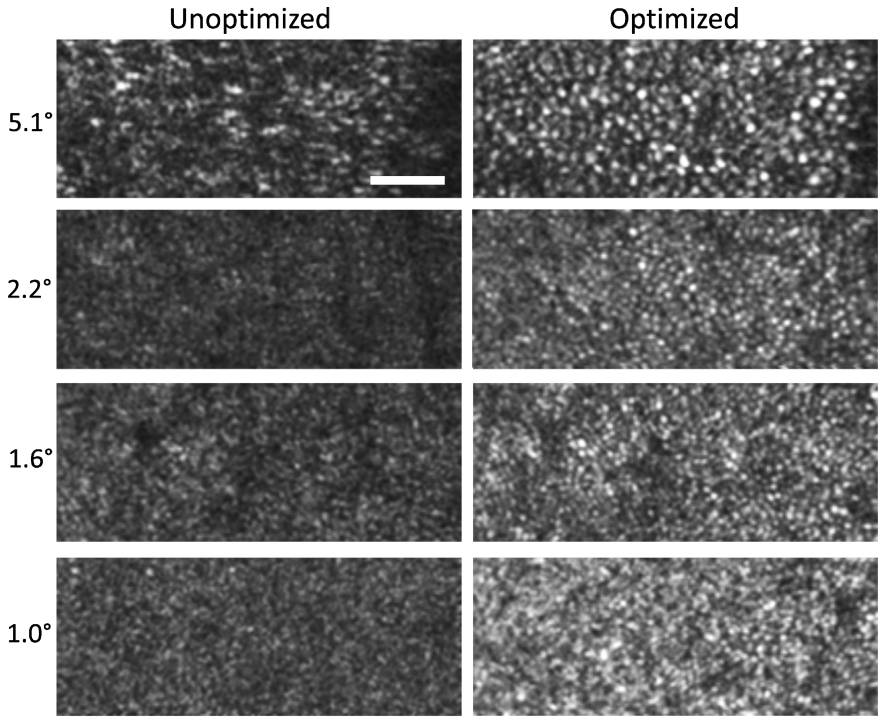

Fig. 6. Images of the photoreceptor mosaic acquired along the superior meridian in a non-mydriatic pupil. These include results acquired at four retinal eccentricities for comparison centered at: 5.1°, 2.2°, 1.6°, and 1.0°. The field of view is 1.0°x0.4° for all images. Scale bar is 50 μm.

4. Discussion and conclusion

We have demonstrated real-time WSAO-OCT for human retinal imaging using a lens-based optical imaging system and a modal optimization algorithm. The real-time optimization was enabled by our ultrahigh-speed GPU-based processing platform. For validation, we presented the improvements in the quality of human photoreceptor mosaic images acquired with OCT after WSAO optimization. With WSAO-OCT, we demonstrated the ability to visualize the photoreceptor mosaic at eccentricities as small as 1°.

WSAO-OCT is potentially advantageous for cellular resolution retinal imaging in cases where wavefront sensing is unreliable. Although the slower convergence time of WSAO-OCT compared to conventional WFS-based imaging means that it cannot currently correct tear film dynamics, in clinical imaging there are often other barriers to AO imaging. For example, wavefront sensing is often compromised by the design and performance of the wavefront sensor detector, not well-defined AO reference plane (over areas of a diseased retina or at the optic nerve head), or light reflected during scanning from optical surfaces in the imaging system. Clinically, the presence of irregular pupils and irregular retinal structures, cataracts or increased opacity in the eye also affects the reliability of the wavefront data. In cases such as these where the accuracy of wavefront measurements is limited, WSAO-OCT could potentially be used to obtain high-resolution images, as WSAO-OCT is only dependent on the acquired image, and not the wavefront measurement.

Another advantage of WSAO-OCT imaging is that it doesn't require a well-defined conjugate plane for successful wavefront sensing. This underlying characteristic should enable WSAO-OCT to perform reliably with high resolution even near non-planar retinal structures, such as the optic nerve head or retinas distorted by pathological changes.

In this research, experiments with the WSAO-OCT system were performed on subjects with non-mydriatic pupils as a proof-of-concept; a larger study in collaboration with ophthalmic clinicians on mydriatic patients was left for future work. Some changes to our current system are required to accommodate the clinical environment. The modal control wavefront sensorless algorithm allows for rapid optimization; however, its convergence time is longer compared to conventional sensor-based AO ophthalmic imaging systems. Motion artifacts during the WSAO optimization process will affect the quality of the aberration correction, and any micro-fluctuations in the ocular aberrations caused by changes in the tear film cannot be accounted for and corrected with the setup reported in this manuscript. Although we were able to reduce the convergence time to 6-12 sec by increasing the image acquisition rate and decreasing the number of corrected Zernike modes, further improvement is desirable. One potential method of decreasing the optimization time is to use faster imaging systems, such as megahertz OCT [47–49], which would increase our current frame rate by 5-10 times. Algorithmic improvements such as real-time blink detection and/or pupil tracking are also potential solutions to reducing the effect of motion artifacts.

In this report, we chose to focus on the photoreceptor layer to showcase the capability of WSAO-OCT. As the computational power of available GPUs continues to grow, a real-time segmentation algorithm could be added, which would enable layer-specific aberration correction. This may also be beneficial for visualizing retinal layers that have a weaker scattering signature, such as the inner and outer nuclear layers.

Finally, to improve the lateral resolution and visualize smaller cellular structures in the retina, such as rod photoreceptor cells and foveal cones, we would need to increase the NA. This would require the use of topical mydriatic agents such as phenylephrine and tropicamide to dilate the pupil in order to enable imaging with a larger diameter beam. An additional benefit of using tropicamide is that it induces cycloplegia in the subject's eye, resulting in a loss of accommodation reflexes that might otherwise interfere with the optimization algorithm. However, imaging with a higher NA introduces additional ocular aberrations and will require a DM with a larger stroke and a higher number of segments for successful aberration correction in both lower and higher order Zernike modes. Alternatively, a woofer-tweeter DM configuration for separating the lower and higher order Zernike modes to two different DMs could be used to augment the aberration-correction ability of our experimental setup [50–53].

In summary, we have demonstrated a lens-based approach for WSAO-OCT that is capable of resolving the cone mosaic in the human eye at small angles of eccentricity with non-mydriatic pupils even with a small-stroke DM. Most importantly, the reduced complexity of the lens-based WSAO design can facilitate a robust and compact imaging system that is highly suitable for clinical applications in ophthalmology.

Acknowledgments

We acknowledge funding for this research from Canadian Institutes of Health Research, Natural Sciences and Engineering Research Council of Canada, Michael Smith Foundation for Health Research, and Simon Fraser University Vice President of Research. R.J. Zawadzki was supported by the National Eye Institute (R01 EY024239), UC Davis RISE Grant, NSF I/UCRC CBSS Grant. The help of John S. Werner and Edward N. Pugh from UC Davis is greatly appreciated. Lastly, we acknowledge NVIDIA for their donation of the Quadro K6000 GPUs.